Phys Chem Minerals (2014) 41:347–359
DOI 10.1007/s00269-013-0654-9

ORIGINAL PAPER

Theoretical study of the local charge compensation and spectroscopic properties of B-type carbonate defects in apatite

Haohao Yi · Etienne Balan · Christel Gervais · Loïc Ségalen · Marc Blanchard · Michele Lazzeri

Received: 18 October 2013 / Accepted: 24 December 2013 / Published online: 10 January 2014

Abstract The structure and spectroscopic properties of selected models of B-type carbonate defects in apatite locally compensated by fluoride or hydroxyl ions are investigated using first-principles quantum mechanical calculations. Theoretical infrared absorption spectra and ^{13}C, and ^{19}F nuclear magnetic resonance chemical shifts are determined. Among the investigated models, only the clumped (CO_3^{2-}, F^-) defect, with the carbonate group close to the sloping face of the tetrahedral site and the F^- ion at the remaining apex, corresponds to previous experimental observations performed on carbonate-fluorapatite samples. Although the substitution of hydroxyl by fluoride ions is commonly observed in minerals, the clumped (CO_3^{2-}, OH^-) defects are unlikely to occur in apatite, considering both their theoretical spectroscopic properties and relative stability. Anionic F^- for OH^- exchange between channel and B sites displays a preference of ~20 kJ/mol for the local charge compensation by fluoride ions at the B-site, pointing to a significantly different behavior of F^- and OH^- ions in the charge compensation mechanism. This difference is ascribed to the poor H-bond acceptor character of available oxygen atoms surrounding the apex of the tetrahedral site. The explicit calculation of the infrared absorption spectra of the defect models is also used to interpret the significant difference observed in the linewidth of the ν_2 and ν_3 CO_3 infrared powder absorption bands of carbonated apatite samples. It is shown that for a concentration of 4.4 wt% of CO_2, long-range electrostatic effects already significantly contribute to the broadening of the ν_3 CO_3 bands in apatite.

Keywords Apatite · Carbonate substitution · First-principles · DFT · FTIR · NMR

Introduction

Apatite is a ubiquitous accessory phase in igneous, metamorphic and sedimentary rocks. It is the major constituent

H. Yi · E. Balan (✉) · M. Blanchard · M. Lazzeri
Sorbonne Universités, UPMC Univ Paris 06, UMR 7590, IMPMC, 75005 Paris, France
e-mail: Etienne.Balan@impmc.upmc.fr

H. Yi · E. Balan · M. Blanchard · M. Lazzeri
CNRS, UMR 7590, IMPMC, 75005 Paris, France

H. Yi · E. Balan · M. Blanchard · M. Lazzeri
IRD, UMR 206, IMPMC, 75005 Paris, France

C. Gervais
Sorbonne Universités, UPMC Univ Paris 06, UMR 7574, Chimie de la Matière Condensée de Paris, 75005 Paris, France

C. Gervais
CNRS, UMR 7574, Chimie de la Matière Condensée de Paris, 75005 Paris, France

C. Gervais
Collège de France, UMR 7574, Chimie de la Matière Condensée de Paris, 75005 Paris, France

L. Ségalen
Sorbonne Universités, UPMC Univ Paris 06, UMR 7193, ISTEP, Biominéralisations et Environnements Sédimentaires, 75005 Paris, France

L. Ségalen
CNRS, UMR 7193, ISTEP, 75005 Paris, France

of some carbonatite and anorthosite (Knudsen and Gunter 2002). Sedimentary apatite deposits, referred to as phosphorites, are the main natural resources in phosphorus (McConnell 1973; Dymek and Owens 2001). Apatite also occurs as the principal inorganic component of bones and dental enamel of vertebrates (Elliott 2002). This motivates active researches for biomedical applications, whereas other technological applications include the storage of radioactive wastes and the production of fertilizers, detergents and phosphoric acid (McConnell 1973; Hughes and Rakovan 2002).

The flexibility of apatite structure enables significant variations of its chemical composition. Anionic substitutions lead to modifications of the chemical occupation of channel sites (F, OH and Cl) and to the incorporation of significant amounts of carbonate in geological and biological samples (Elliott 1994, 2002). The carbonate ion can substitute in the phosphate tetrahedral site (B-type carbonate defect) or in the structural channels centered on the hexagonal symmetry axis (A-type carbonate defect). Depending on the formation conditions of apatite, FTIR and NMR spectroscopic investigations (e.g., Regnier et al. 1994; Michel et al. 1995; Tacker 2008; Mason et al. 2008, 2009; Fleet 2009) reveal the occurrence of these various modes of carbonate incorporation. Inferences from spectroscopic observations are also supported by structure refinements using X-ray or neutron diffraction (e.g., LeGeros 1965; Schuffert 1990; Leventouri et al. 2000; Wilson et al. 1999, 2004, 2006) although the small grain size and twinning of low-temperature apatite samples appear as limiting factors. More recently, single-crystal structure refinements performed on high-quality apatite crystals synthesized under high-pressure conditions shed light on the structural environment and incorporation mechanisms of carbonate groups in apatite (Fleet and Liu 2004, 2007, 2008; Fleet 2009; Fleet et al. 2011).

The carbonate for phosphate substitution in the apatite structure requires adding a negative charge to maintain the local electrostatic balance. A number of potential charge-compensating mechanisms have been suggested, corresponding to various subtypes of B-type carbonate defects (e.g., Ivanova et al. 2001; Wilson et al. 2004; Nokhrin et al. 2006; Antonakos et al. 2007).

In low-temperature carbonated fluorapatite samples ("francolite"), the observation of excess fluorine ions has led to the proposal that the carbon for phosphorus substitution is coupled to a fluorine for oxygen substitution (e.g., McClellan and Lehr 1969). Local charge compensation of carbonates by F^- or OH^- ions, resulting in the formal species $(CO_3OH)^{3-}$ and $(CO_3F)^{3-}$, has been considered early because F^- and OH^- ions naturally occur in the apatite structure (e.g., Elliott 1964; McClellan and Lehr 1969; Vignoles et al. 1988; Binder and Troll 1989). However, the local character of the charge compensation has been further questioned by several theoretical and experimental studies (e.g., Regnier et al. 1994, 1996; Pan and Fleet 2002; Mason et al. 2009). The existence of a clumped (CO_3^{2-}, F^-) defect in natural carbonated fluorapatite ("francolite" type carbonate) has been recently confirmed by direct spectroscopic observations and theoretical modeling (Yi et al. 2013).

In comparison, carbonate incorporation at the B-site of F-free hydroxyapatite seems to systematically involve more complex mechanisms. For example, Rietveld refinement of X-ray diffraction patterns of synthetic or biologic carbonate-bearing apatite samples has suggested that Ca vacancies may compensate the charge imbalance, although the position of the vacancies with respect to the carbonate group remains uncertain (e.g., Wilson et al. 1999, 2006; Ivanova et al. 2001). Pasteris et al. (2012) observed a correlation between incorporation of carbonate at B-site and depletion of channel OH groups. A coupled substitution involving parallel replacement of Na^+ for Ca^{2+} was also proposed on the basis of compositional data from natural carbonate-bearing apatites (McConnell 1952; Ames 1959) and has been confirmed by the synthesis of Na and carbonate-bearing apatites (e.g., Bonel et al. 1973; Fleet and Liu 2008). More specifically, a coupled mechanism involving both A-type carbonate groups and Na for Ca substitution has been proposed from structure determination of A–B apatite single crystals (Fleet 2009). Such mechanism is supported by the observation of characteristic ratios of Na to A and B carbonates. Although the role of A-type carbonate in the charge compensation of B-type carbonate is not intuitively obvious, it is explained by the steric repulsion between the channel carbonate oxygen atom and neighboring phosphate oxygen atom, promoting the formation of an oxygen vacancy at the tetrahedral site (Fleet 2009). In natural samples, other coupled substitutions, e.g., involving a concomitant replacement of SiO_4^{4-} for PO_4^{3-}, have been established on the basis of compositional data from high-temperature carbonate-bearing apatite in igneous rocks (e.g., Sommerauer and Katz-Lehnert 1985; Comodi et al. 1999).

Interestingly, the carbonated fluorapatite samples investigated by Fleet (2009) display a B/A ratio >1 and a spectroscopic signature that could be ascribed to isolated carbonate groups. In comparison, high-pressure synthetic hydroxyapatite samples display a B/A ratio <1. This contrasted behavior is somehow surprising because the fluorine for hydroxyl substitution is commonly observed in minerals and synthetic compounds (e.g., Robert et al. 1999, 2013) and the charge compensation of cationic vacancies by protons is a usual incorporation mechanism of OH groups in nominally anhydrous minerals (e.g., Bell and Rossman 1992; Keppler and Smyth 2006). In addition, simple electrostatic considerations suggest that local electrostatic

charge compensation mechanisms are energetically more favorable than more remote mechanisms. Therefore, there is no obvious reason explaining why hydroxyl ions would be less efficient than fluoride ions for the local charge compensation of B-type carbonate groups in apatite.

In the present study, we compare the respective roles of fluoride and hydroxyl ions in the local charge compensation of carbonate at B-site, using a first-principles theoretical modeling approach. Computational simulations can indeed provide important information on the atomic-scale structure of carbonate defects in apatite (e.g., Peeters et al. 1997, Astala and Stott 2005, Rabone and de Leeuw 2007, de Leeuw 2010, Ulian et al. 2013a, b), and the theoretical modeling of spectroscopic properties makes it possible to test atomic-scale models of defects in minerals against experimental observations (e.g., Balan et al. 2013). After a detailed presentation of the clumped (CO_3^{2-}, F^-) defect recently recognized in natural fluorapatite samples (Yi et al. 2013), we determine the theoretical structural, nuclear magnetic and vibrational properties of stable models of clumped (CO_3^{2-}, F^-) and (CO_3^{2-}, OH^-) defects in apatite and we discuss the specificity of OH groups as charge-compensating species. Finally, theoretically determined infrared absorption properties are used to explain the contrasted characters of the ν_2 and ν_3 CO_3 absorption bands observed in the infrared spectrum of many synthetic or natural apatite samples.

Theoretical methods

The stable structure and spectroscopic properties of models of carbonate-substituted apatite were computed within the density functional theory (DFT) framework, using the generalized gradient approximation (GGA) for the exchange-correlation functional as proposed by Perdew et al. (1996). The structural and vibrational calculations were performed using the PWscf and PHonon codes of the Quantum Espresso package (Giannozzi et al. 2009). The ionic cores of Ca, P, O, F and H were described by ultra-soft pseudo-potentials from the Quantum Espresso library (http://www.quantum-espresso.org). The electronic wave functions and charge density were expanded in plane waves using 50 Ry and 500 Ry cutoffs, respectively. Models of carbonate defect were built by incorporating one carbonate group in a fluorapatite primitive cell (42 atoms). The cell parameters were fixed at the theoretical relaxed cell parameters of pure fluorapatite ($a = 9.48$ Å, $c = 6.90$ Å; Balan et al. 2011). The sampling of the Brillouin zone for the electronic integration was restricted to a single k-point (−.5, −.87, −.68; in Cartesian coordinates and 2π/a units). The fixed-cell optimization of atomic positions was done until the residual forces were less than 10^{-4} Ry/a.u. The harmonic low-frequency dielectric tensor (Baroni et al. 2001) of the theoretical equilibrium structure was calculated following the procedure described in previous studies (e.g., Balan et al. 2001, 2011).

The NMR chemical shifts were obtained on the same structural model by calculating the shielding of the nuclei relative to the electronic current induced by the external magnetic field. This current was calculated using the GIPAW approach, which allows reconstructing the all-electron magnetic response from the pseudo-wave functions (Pickard and Mauri 2001). The calculations were performed using the PWscf and GIPAW codes of the Quantum Espresso package (Giannozzi et al. 2009). For this calculation, norm-conserving pseudo-potentials were used and the wave functions kinetic energy cut-off was increased to 80 Ry. The integral over the Brillouin zone was done using a Monkhorst-Pack 2 × 2 × 2 k-point grid. The isotropic chemical shift σ_{iso} is defined as $\sigma_{iso} = -(\sigma - \sigma^{ref})$, where σ is the isotropic shielding (one-third of the trace of the NMR shielding tensor) and σ^{ref} is the isotropic shielding of the same nucleus in a reference system. In our calculations, absolute shielding tensors are obtained. To fix the scales, σ^{ref} was chosen by comparing experimental and calculated σ^{iso} values in calcite ($CaCO_3$) for ^{13}C and in fluorapatite ($Ca_5(PO_4)_3F$) for ^{19}F. It should be noticed that for ^{19}F, a scaling factor $k = 0.68$ was applied since previous GIPAW calculations recommended this correction to obtain accurate predictions (Griffin et al. 2010).

Results

Theoretical models of carbonate defects in apatite

The B-type models correspond to the substitution of a CO_3^{2-} group for a PO_4^{3-} group in the apatite structure. The corresponding defects have a positive charge that requires a charge balance mechanism. Models B_H and B_F involve a local charge compensation of the carbonate defect by a monovalent anionic species, OH^- and F^- ions, respectively. Additional calculations were performed on the A-type carbonate to enable a thorough comparison of its spectroscopic properties with those of the B-type models. The relaxed structure of B- and A-type models is displayed in Figs. 1, 2, 3 and 4, in which the atom labeling follows usual conventions for apatite, whereas oxygen atoms belonging to carbonate groups are labeled following Fleet and Liu (2008). Note that Yi et al. (2013) used an unconventional labeling of atoms, differing from that in the present study.

The model B_F has been briefly described in Yi et al. (2013). Using the fluorapatite primitive cell, the distance between image carbonate groups due to periodic boundary conditions is larger than 6 Å. Calculations of the B_F model using a 2 × 2 × 2 apatite super-cell lead to a nearly identical

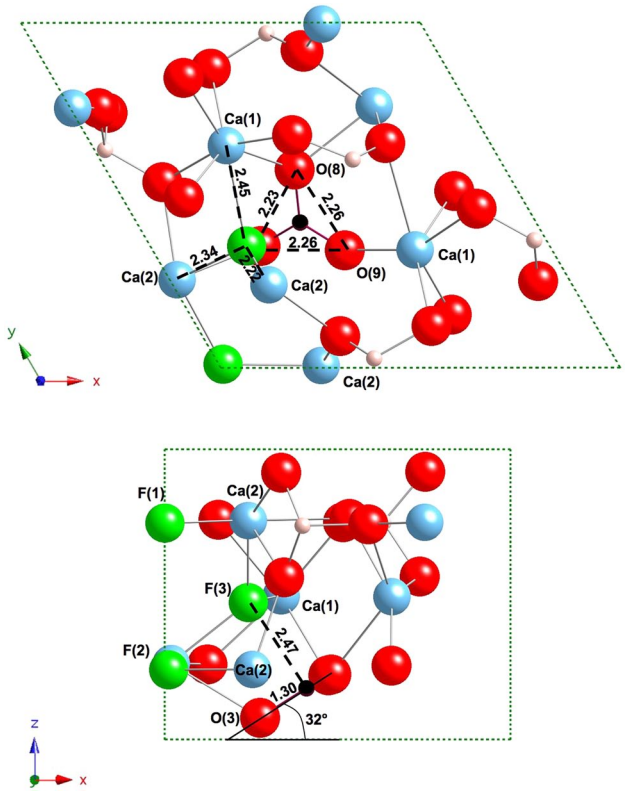

Fig. 1 Theoretical model of B-type carbonate locally compensated by a fluoride ion (B_F model) in fluorapatite (O = *red*, F = *green*, P = *light pink*, C = *black*, Ca = *light blue*). *Top*: view along the *c*-axis. *Bottom*: view along the *b*-axis. Selected distances are indicated in Å. The model is identical to that discussed by Yi et al. (2013)

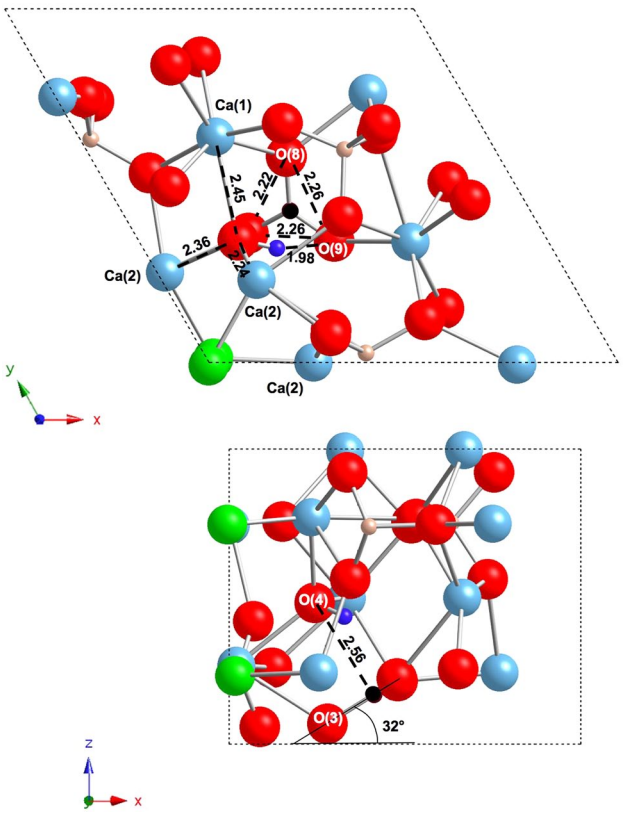

Fig. 2 Theoretical model of B-type carbonate locally compensated by an OH^- group (B_H_1 model) in fluorapatite (O = *red*, F = *green*, P = *light pink*, C = *black*, Ca = *light blue*, H = *deep blue*). *Top* view along the *c*-axis. *Bottom* view along the *b*-axis. Selected distances are indicated in Å. The OH^- group points to the O(9) atom of the carbonate group

geometry and orientation of the carbonate group, with modifications of interatomic distances smaller than 0.01 Å. This large-cell (336 atoms) calculation confirms that the interaction between the periodic images of the carbonate defect is already weak in the primitive-cell model. Primitive-cell models of neutral carbonate defects with local charge compensation thus provide a realistic picture of these carbonate defects, consistent with the previous findings of Ulian et al. (2013a). It should be also noted that the concentration of ~4.4 wt% of CO_2 considered in the primitive-cell models is not unrealistic (e.g., McClellan and Lehr 1969). In contrast, defect models involving remote charge compensation mechanisms or the use of a homogeneous charge-compensating electrostatic background require larger super-cell to achieve a full convergence of the defect properties (Astala and Stott 2005).

In the B_F model (Fig. 1), the carbonate group is located on the basal face of the tetrahedral site, forming an angle of 32° with respect to (001) plane. The C–O bond lengths (Table 1) range between 1.294 Å (C–O(9)) and 1.306 Å (C–O(8)), leading to O–O distances ranging between 2.23 and 2.26 Å. Compared with the phosphate-occupied tetrahedral site, the carbonate group substitution leads to a contraction of the basal face (theoretical O–O distances of the phosphate site range between 2.49 and 2.57 Å; Balan et al. 2011) and a ~3° tilt away from the phosphate tetrahedron. The theoretical isolated B_F carbonate defect thus displays a smaller distortion but a tilt angle very similar to that experimentally determined for the carbonate group in A–B fluorapatite (Fleet and Liu 2008). This tilt angle significantly differs from that observed in Na-bearing hydroxyapatite, which reaches 18° (Fleet and Liu 2007). The local electrostatic charge compensation of the defect is ensured by a fluoride ion located at the remaining apex of the tetrahedral site, thus corresponding to the substitution of a fluorine for an O(3) atom. The environment of the fluoride ion is similar to that previously suggested for excess fluoride anion in high-pressure synthesized fluorapatite and authigenic francolite by Fleet and Liu (2008). The distance between the fluoride ion and the carbon atom is 2.47 Å. This distance is significantly larger than the expected C···F distance for a bonded interaction (e.g., 1.46 Å from ionic radii, Shannon 1976), whereas the planar carbonate geometry attests for the sp2 hybridization of carbon. Thus, the clumping of

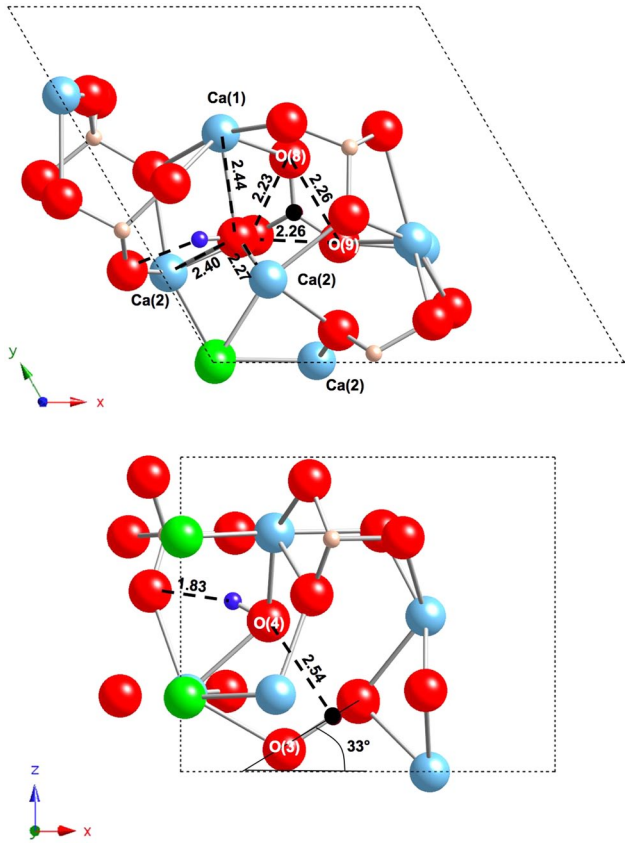

Fig. 3 Theoretical model of B-type carbonate locally compensated by an OH^- group (B_H_2 model) in fluorapatite (O = *red*, F = *green*, P = *light pink*, C = *black*, Ca = *light blue*, H = *deep blue*). *Top* view along the *c*-axis. *Bottom* view along the *b*-axis. Selected distances are indicated in Å. The OH^- group points to the O(3) atom of a neighboring phosphate group

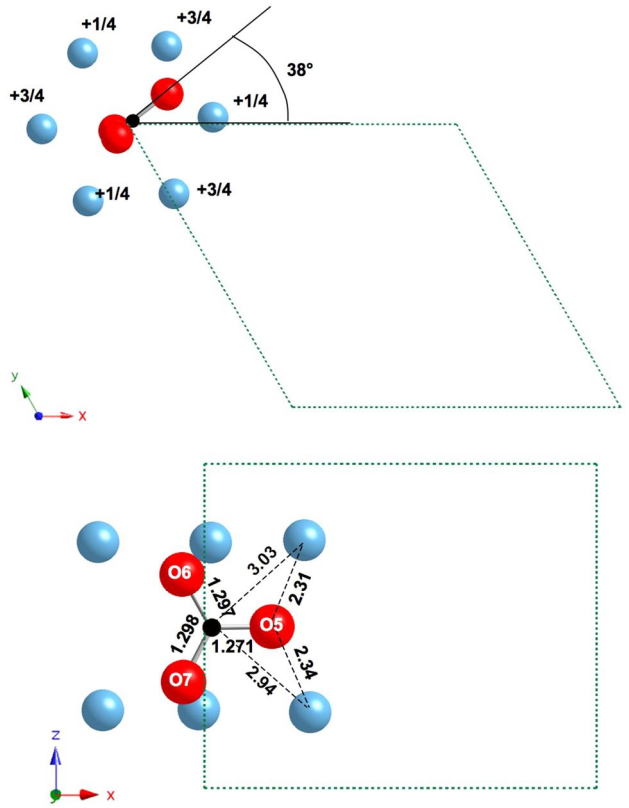

Fig. 4 Theoretical model of A-type carbonate in fluorapatite (O = *red*, C = *black*, Ca = *light blue*). *Top* view along the *c*-axis. The *z* coordinate of Ca atoms is indicated. *Bottom* view along the *b*-axis. Selected distances are indicated in Å. In this case, no charge compensation is required as the carbonate group replaces two OH^- groups

carbonate and fluoride ions in fluorapatite does not involve any direct bonding between the two species. However, the fluoride ion is still located at a crystal site. It is shifted by only 0.4 Å from the position of the O(3) atom in the phosphate-occupied tetrahedral site. It does not migrate to the interstitial position previously observed in the modeling of a carbonate-fluorapatite cluster (Regnier et al. 1994).

For comparison, two configurations of clumped (CO_3^{2-}, F^-) defects with the carbonate group located on one of the nonequivalent vertical faces of the PO_4 tetrahedron and the fluorine ion at the remaining apex have been also investigated. They are referred to as B_F_V_1 and B_F_V_2, corresponding to a carbon location at the center of the (O(8), O(3), O(3)) or (O(9), O(3), O(3)) triangles, respectively (Table 1). Although stable, they were found to be less favorable than the B_F model by 18 kJ/mol (B_F_V_1) and 10 kJ/mol (B_F_V_2). This is consistent with experimental observations indicating that the CO_3 groups are preferentially located on the sloping faces of the tetrahedral sites of apatite (Elliott 1994; Suetsugu et al. 1998; Fleet 2009).

Table 1 Selected bond lengths of relaxed theoretical models of carbonate fluorapatite

	d C-O(3) (Å)	d C-O(8) (Å)	d C-O(9) (Å)	d C…F (Å)	d OH (Å)
B_F	1.299	1.306	1.294	2.47	–
B_F_V_1	1.295	1.311	–	2.51	–
B_F_V_2	1.302	–	1.302	2.45	–
B_H_1	1.295	1.299	1.303		0.972
B_H_2	1.301	1.303	1.293		0.978

In the models of B_H type, the fluoride ion of model B_F is replaced by a hydroxyl group pointing toward the center (B_H_1) or the outside (B_H_2) of the tetrahedral site. The model B_H_1 is more stable than model B_H_2 by ~27 kJ mol^{-1}.

In model B_H_1 (Fig. 2), the OH group points toward the oxygen O(9), which displays the longest distance to the carbon atom (1.303 Å). The carbonate geometry (Table 1) and orientation is still close to that observed for the B_F model. The O(H)···C distance is 2.56 Å, slightly longer than the F···C distance in model B_F. A relatively short

O–H bond length of 0.972 Å is observed, with O(H)···O and (O)H···O distances of 2.85 and 1.98 Å, respectively. Attempts to locate the H atom between O(4) and O(8) or between O(4) and O(3) did not lead to stable configurations, and the corresponding models always relaxed to a configuration with the OH group pointing toward O(9). The B_H_1 defect geometry differs from that of the equivalent defect in hydroxyapatite previously obtained using empirical potentials (Peroos et al. 2006). In this last case, the hydrogen-bond interaction involves two oxygen atoms of the carbonate group with (O)H···O bond distances between 2.15 and 2.41 Å.

After relaxation, the B_H_2 defect (Fig. 3) displays two almost identical C–O bond lengths at 1.302–1.303 Å and a third shorter C–O(9) bond (1.294 Å; Table 1). The O(H)···C distance is similar to that of B_H_1 at 2.54 Å. The OH group points to the O(3) oxygen of a neighboring phosphate group. Its length is 0.979 Å, slightly longer than in model B_H_1 and consistent with a shorter O(H)···O distance of 2.74 Å.

In addition, four models of clumped (CO_3^{2-}, OH^-) defects with the CO_3 group vertically orientated and the OH group pointing inward or outward the tetrahedral site have been investigated. All the relaxed configurations were less favorable than the B_H_1 model, by 22 to 66 kJ/mol. As for the B_H_1 and B_H_2 models, the outward configurations were significantly less stable (by ~40 kJ/mol) than their inward counterparts.

Constant-volume calculations of the structure of B-type defects were also performed using a hydroxyapatite primitive cell. These calculations lead to very similar orientation and geometry of the defects. For example, the B_F defect in hydroxyapatite displays a C···F distance of 2.48 Å and an angle of 33° with respect to the (001) plane. Mutual substitution of OH^- and F^- ions in apatite channel is thus not expected to significantly affect the isolated B-type carbonate defects. The energy change related to the exchange of OH^- and F^- ions between channel and B-site positions was calculated in the fluorapatite and hydroxyapatite cells. In both cases, a configuration with the OH group at the channel site and the F ion at the B-site is preferred by about 17 kJ/mol (in fluorapatite) to 22 kJ/mol (in hydroxyapatite). In comparison, the OH for F substitution in channel sites only displays a small stabilization (2.3 kJ/mol) of the mixed configuration with respect to an equivalent mixture of the pure end-members. For this last calculation, the system cell parameters were free to relax. Although consistently negative, the stabilization energy is slightly smaller than the 7 kJ/mol value obtained by De Leeuw et al. (2002) using the Perdew-Wang GGA functional.

The relaxed structure of the A-type model is in good agreement with the results of the previous theoretical works of Peeters et al. (1997), Astala and Stott (2005) and Ulian et al. (2013a). The carbonate molecule is nearly vertically oriented with one C–O bond perpendicular to the c-axis of apatite structure and the carbon position at $z = 0.5$ (Fig. 4). The carbonate group is nearly symmetric with respect to the (001) plane. The C–O distances are 1.27 Å for the horizontal C–O(5) bond and 1.30 Å for the two other bonds. The corresponding average C–O bond length (1.29 Å) is identical to that previously determined by Ulian et al. (2013a) using the B3LYP functional.

Theoretical NMR results

The theoretical ^{13}C and ^{19}F NMR parameters of B-type defect in fluorapatite are summarized in Table 2 together with the experimental values reported for fluorinated apatites, francolite (Yi et al. 2013) and stafellite (Mason et al. 2009), as well as ^{13}C parameters reported for synthetic carbonated hydroxyapatites (Beshah et al. 1990).

Considering the B-type carbonate models, ^{13}C calculated values are close to 170 ppm, in good agreement with the experimental data. We note, however, that the B_F_V_1 and B_F_V_2 models, which display vertically orientated carbonate groups, lead to slightly overestimated values (>171 ppm). The calculated ^{13}C value for the A-type model is 164.7 ppm, slightly underestimated compared to its experimental counterparts (165.5 ppm, Beshah et al. 1990;

Table 2 Theoretical and experimental ^{13}C and ^{19}F NMR chemical shift (ppm) of carbonate fluorapatite

	B_H_1	B_H_2	B_F	B_F_V_1	B_F_V_2	A	B-type exp.	A-type exp.	Channel F exp.	B-site F exp.
^{13}C	170.8	170.7	169.8	171.4	171.7	164.7	170±1[a,b,c]	165.5[a] 168.6[b]	–	–
^{19}F	−100.3	−100.7	−102.1	−105.0	−107.2	–	–	–	−102[c] −99.8[b]	–
	−103.2	−104.1	−103.3	−102.2	−102.6	–	–	–		–
	–	–	−84	−67.5	−76.5	–	–	–	–	−88[c] −86.6[b]

[a] Beshah et al. (1990)

[b] Mason et al. (2009)

[c] Yi et al. (2013)

168.6 ppm, Mason et al. 2009). A calculation using a double cell size along the c-axis, ensuring a separation of the A-type channel carbonate ions by fluorine ions, insignificantly changed the ^{13}C chemical shift to 165 ppm.

The ^{19}F chemical shift parameters cover a larger range from −67.5 ppm in model B_F_V_1 to −104.1 ppm in model B_H_2. In all models, one at least of the fluorine sites (located in the structural channels) shows a chemical shift around −102 ppm consistent with the experimental ^{19}F parameters of pure fluorapatite (Yi et al. 2013). In the models B_H_1 and B_H_2, the other channel site is calculated around −100 ppm. In model B_F, the chemical shift of the fluoride ion located at the B-site is computed at −84.0 ppm. It is experimentally observed around −86.6 ppm in the "stafellite" sample investigated by Mason et al. (2009) and −88 ppm in the "francolite" sample of Yi et al. (2013). Interestingly, the two less stable fluorinated models with a vertical orientation of the carbonate group lead to ^{19}F chemical shifts of −67.5 and −76.5 for the B_F_V_1 and B_F_V_2 models, respectively. This corresponds to a significantly poorer agreement with experimental observations.

The occurrence of clumped (CO_3^{2-}, F^-) defects with vertically orientated carbonate groups can therefore be ruled out both from energetic considerations and from the lack of agreement with NMR spectroscopic observations. Considering that the clumped (CO_3^{2-}, OH^-) defects with vertically orientated carbonate groups are significantly less stable than the chemically equivalent B_H_1 model and that experimental observations consistently indicate that B-type carbonate groups in hydroxyapatite occupy the sloping faces of the tetrahedral sites (e.g., Wilson et al. 2004, 2006; Fleet 2009), models with vertically orientated carbonate groups will not be considered in any further details in the present study.

Theoretical vibrational properties of carbonate defects in apatite

The vibrational transverse optical (TO) modes (using the definition given by Baroni et al. (2001), i.e., the modes coupled with a zero macroscopic electric field) of the defective apatite structure (models B_F, B_H_1, B_H_2 and A) have been obtained by diagonalization of the theoretical dynamical matrix (Table 3). Compared with experimental ones, the theoretical frequencies of apatite are underestimated by about 5%, an effect related to the use of the generalized gradient approximation to the exchange-correlation functional (e.g., Balan et al. 2011). The commonly observed IR-active vibrational modes of carbonate in apatite are related to the antisymmetric stretching of C–O bonds (ν_3 modes) and to the motion of the C atom perpendicularly to the plane of the carbonate molecule (ν_2 out-of-plane bending mode). In all cases, these ν_2 and ν_3 internal modes are well defined and do not display any significant contribution from the phosphate groups of the host structure.

In apatite, the twice-degenerated ν_3 modes of the free carbonate ion are split by the site distortion. The ν_3 CO_3 stretching modes are calculated between 1,300 and 1,600 cm^{-1}. The splitting is significantly larger for the A-type model (90 cm^{-1}) than for B-type models (from 14 cm^{-1} in B_H_1 to 40 cm^{-1} in B_F). The B_H_2 model, in which the OH group points out of the tetrahedral site, and the fluorinated B_F model display very similar ν_3 CO_3 wavenumbers. The ν_3 CO_3 wavenumbers are in fact broadly correlated to the involved C–O bond length (Fig. 5). The high-frequency ν_{3b} component is related to the vibration of the shorter C–O bond, whereas the low-frequency ν_{3a} component involves the coupled motion of the two remaining longer C–O bonds. Consistent with the experimental observations of Suetsugu et al. (1998), the ν_{3b} band of the A-type defect, which involves the shorter C–O(5) bond, is polarized perpendicularly to the c-axis. The average ν_3 CO_3 wavenumber (Table 3) of the A-type defect (1,467 cm^{-1}) is significantly higher than that of B-type defects (~1,400 cm^{-1}), reflecting the comparatively shorter average C–O bond length of the A-type defect. This 67 cm^{-1} shift is consistent with the one experimentally observed between the ν_3 mode of B-type (1,443 cm^{-1}, Regnier et al. 1994)

Table 3 Theoretical transverse optical frequency and IR cross section (in parentheses, $(D/Å)^2/amu$) of selected vibrational modes of carbonate fluorapatite. Experimental frequencies are reported for comparison

	ν_2 CO_3 (cm^{-1})	ν_{3a} CO_3 (cm^{-1})	ν_{3b} CO_3 (cm^{-1})	ν_3 CO_3 average (cm^{-1})	Splitting of $\nu_3 CO_3$ (cm^{-1})	OH stretching
B_H_1	771 (9.68)	1,396 (26.5)	1,410 (26.2)	1,403	14	3,697
B_H_2	807 (4.74)	1,379 (25.9)	1,418 (30.5)	1,398.5	39	3,578
B_F	813 (4.11)	1,376 (27.2)	1,416 (30.9)	1,396	40	–
B Exp.*	864 –866	1,400–1,440	1,450–1,470	–	25–50	–
A	826 (3.65)	1,422 (25.0)	1,512 (25.8)	1,467	90	–
A Exp.*	878–880	1,450–1,470	1,540–1,550	–	70–100	–

* Suetsugu et al. (1998); Tacker (2008); Yi et al. (2013)

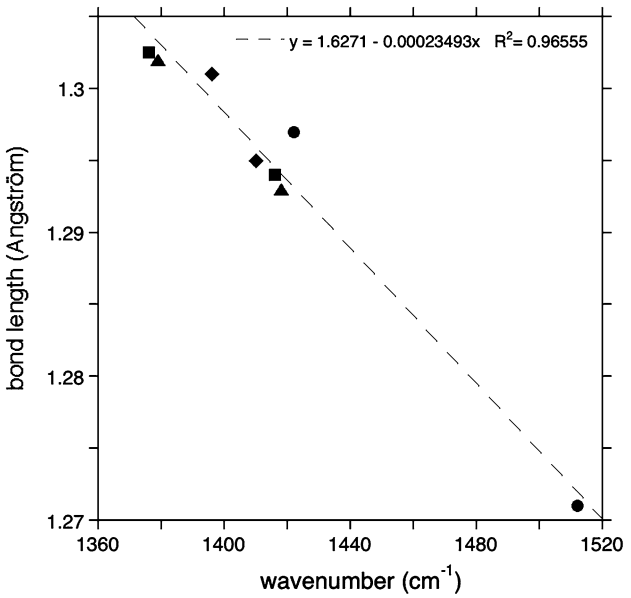

Fig. 5 Correlation between the wavenumber of the ν_3 CO_3 modes and the length of C–O bonds. *circles*: A-type, *squares*: B_F, *diamonds*: B_H_1, *triangles*: B_H_2

and A1-type (1,502.5 cm^{-1}; Fleet et al. 2011) carbonates in fluorapatite.

The ν_2 carbonate mode of the B_H_2 and B_F models is calculated at 807 and 813 cm^{-1}, respectively, whereas that of the A-type model is calculated at 826 cm^{-1} (Table 3). The 13 cm^{-1} difference observed between the B_F and A models is consistent with the difference experimentally observed between the B2 and A-type signals in fluorapatite (16 cm^{-1}, Fleet 2009). A significantly lower wavenumber is computed for the B_H_1 model, at 771 cm^{-1}. A contribution involving the OH group of the defect is observed in the ν_2 mode of B_H_1 model and, to a lesser extent, of B_H_2 model.

The change of selected vibrational frequencies has been investigated as a function of the cell volume (Table 4). Approximate values of the mode-Grüneisen parameters were obtained by computing the frequency changes induced by an isotropic increase in the cell parameters of 1 %. The two ν_3 CO_3 stretching modes display positive mode-Grüneisen parameters, consistent with the reverse correlation observed between the C–O stretching frequencies and C–O bond lengths. The ν_2 CO_3 modes of models B_H and B_F display a significant and negative mode-Grüneisen parameter, whose magnitude is larger for the B_H models than for the B_F model. In comparison, the ν_2 CO_3 mode frequency of the A-type model weakly depends on the unit-cell volume.

Finally, we note that the presence of substituted carbonate groups modifies the symmetry of the structure and leads to significant modifications of the vibrational modes of

Table 4 Approximate mode-Grüneisen parameter* of selected vibrational modes of carbonate and phosphate in fluorapatite

Mode	B_H_1	B_H_2	B_F	A	F-apatite
ν_2 CO_3	−0.24	−0.25	−0.16	−0.02	–
ν_{3a} CO_3	0.16	0.31	0.32	0.25	–
ν_{3b} CO_3	0.31	0.17	0.21	0.35	–
ν_1 PO_4	0.40	0.45	0.48	0.41	0.51

* Approximate mode-Grüneisen (1912) parameters, $\tilde{\gamma}_i$, are defined by $\tilde{\gamma}_i = -\frac{V}{\omega_i}\frac{\Delta\omega_i}{\Delta V}$ where $\Delta\omega_i$ is the angular frequency variation of the *i*th vibrational mode induced by a ΔV change of the cell volume

surrounding phosphate groups. However, such effects are expected to lead to modifications of the vibrational properties of the host structure at a relatively long spatial scale and cannot be fully accounted for using the present modeling strategy (see, e.g., Lazzeri and Thibaudeau 2006).

Theoretical infrared absorption spectrum of carbonate fluorapatite

The IR absorption cross sections of IR-active vibrational modes were obtained from the Born effective charge tensors and atomic displacements (Table 3). The two ν_3 CO_3 stretching modes of B- and A-type carbonate models display comparable cross sections with a slightly stronger absorption for the high-frequency component. This suggests that fits of the ν_3 CO_3 stretching modes in unpolarized spectra should be performed by using pairs of absorption bands with similar intensities. A slight enhancement of the ν_3 CO_3 absorption is also observed for the B-type models with respect to the A-type model. The ν_2 CO_3 bending mode of the B_H_2 and B_F models displays a similar cross section, slightly stronger than that of the A model. Such moderate difference is, however, probably difficult to evidence from powder IR absorption experiments, given the uncertainties related to the baseline subtraction and to the fit of partially overlapping contributions from A-type and B-type signals (Fleet 2009). Together with a lower frequency, the ν_2 CO_3 mode of the B_H_1 model displays an absorption cross section significantly stronger than that of the two other B-type models.

Although IR cross sections provide information on the absorption properties of carbonate defects in fluorapatite, it does not fully account for the spectroscopic properties of experimental powder samples. In particular, it does not account for the influence of macroscopic electrostatic effects related to the finite size of the absorbing particles (e.g., Fuchs 1975; Ruppin 1977, 1978). A better description of the IR absorption properties relies on the computation of the dielectric properties of the material, then making it possible to derive a theoretical absorption spectrum for a given experimental setup. In the case of a pure crystal, the dielectric tensor

is obtained from the transverse vibrational modes and Born effective charge tensors (see, e.g., Balan et al. 2001, 2011). In the case of a defective crystal, the determination of the dielectric tensor is not as straightforward because the structural models are obtained using periodic boundary conditions. Two aspects have to be considered when modeling the properties of the defective crystal. First, the dielectric tensor should reflect the fact that the substitution may randomly occur on equivalent sites of the cell. The dielectric tensor of carbonate-bearing apatite is thus expected to display a uniaxial symmetry, even though the periodic model presents a lower symmetry. Second, even though the cell size is sufficient to lead to a realistic local structure and to minimize the interaction between image defects, long-range electrostatic interactions related to the polarization of absorbing defects can still occur.

The proper modeling of these two points raises significant difficulties, and in the following, we adopt a simplified approach in which each aspect is treated separately. First, the potential long-range electrostatic interaction between the defects is neglected, and the absorption spectrum of the defective apatite is computed by simply averaging the perpendicular components ε_{xx} and ε_{yy} of the dielectric tensor

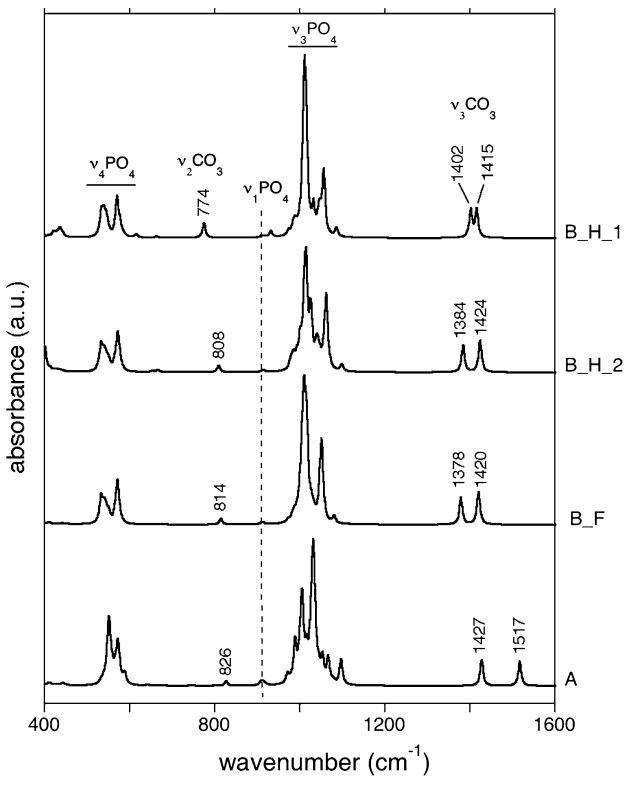

Fig. 6 Theoretical powder infrared absorption spectrum of carbonate apatite models, calculated assuming that spherical apatite particles are inserted in a homogeneous KBr matrix. The wavenumbers of the ν_2 and ν_3 CO_3 modes are indicated. The wavenumber of ν_3 CO_3 modes differs by about 5 cm^{-1} from the corresponding transverse optical mode frequencies (Table 3)

of the defect model, ε_{zz} remaining unchanged and all the nondiagonal components vanished. A theoretical powder infrared absorption spectrum can then be calculated from the averaged dielectric tensor in assuming that isolated spherical apatite particles are inserted in a homogeneous KBr matrix (Fig. 6).

Compared with pure fluorapatite, carbonate defects lower the symmetry of the structure of apatite, leading to new IR-active vibrational modes. As shown in Fig. 6, models with different carbonate defect display very different shape of the intense ν_3 PO_4 vibrational band. The weaker ν_1 PO_4 band is also affected, and five nondegenerated IR-active vibrational modes of the defective apatite structure are related to the ν_1 vibration of the PO_4 group. The corresponding wavenumbers are spread over 5–10 cm^{-1}.

For all the models, macroscopic electrostatic effects affect the intense absorption bands, which are shifted to higher frequency from the corresponding transverse optical frequency (Fig. 6). The ν_3 CO_3 stretching bands are shifted by ~5 cm^{-1}. Compared with bare IR cross sections (Table 3), the relative intensity of the ν_3 CO_3 bands is also affected. The less absorbing ν_2 CO_3 and ν_1 PO_4 bands are less affected by macroscopic electrostatic effects. This is related to the weakness of the associated depolarization field in the absorbing particle. We note, however, that in the case of defects, the macroscopic depolarization field will depend on the defect concentration and that such macroscopic electrostatic effects may increase with the carbonate concentration. As shown by the present calculations, they can already be observed in the investigated system that contains 4.4–4.5 wt% of CO_2.

Independent of the powdered nature of some apatite samples, electrostatic interactions can also occur at a microscopic scale between substituted carbonate groups. This effect can be assessed by considering the dispersion of the carbonate vibrational modes in the investigated models, recalling that vibrational modes at the boundary of the Brillouin zone correspond to out-of-phase vibrations in adjacent cells, whereas those at the center of the Brillouin zone correspond to the in-phase vibration of the whole periodic system. Theoretical phonon frequencies have thus been computed at the high-symmetry K and M points of the

Table 5 Theoretical phonon frequencies (cm^{-1}) computed at the center (Γ) and high-symmetry K and M points of the hexagonal Brillouin zone for model B_F

	Γ	M	K
ν_2 CO_3	813	813	814
ν_{3a} CO_3	1,376	1,389	1,383
ν_{3b} CO_3	1,416	1,420	1,425
ν_1 PO_4	911	911	911

hexagonal Brillouin zone for model B_F (Table 5). The ν_2 CO_3 mode displays a negligible dispersion, consistent with the weakness of the associated polarization and IR absorption cross section. In contrast, the ν_3 CO_3 modes show a significant shift to higher wavenumbers, ranging from 4 to 13 cm^{-1}.

Therefore, at a concentration level of ~4.4 wt% CO_2, the ν_3 CO_3 absorption bands appear as significantly affected by electrostatic effects occurring both at the macroscopic scale in the absorbing particles and at the microscopic scale, due to the random distribution of the defects in the crystal. In comparison, the ν_2 CO_3 and ν_1 PO_4 are less affected and should provide a better insight into the atomic-scale properties of the defective crystal. Although these calculations were performed on model B_F, these observations also stand for the other models because the electrostatic interactions mostly depend on the microscopic polarizability of the carbonate group.

Discussion

Constraints on B-type carbonate incorporation mechanisms

The occurrence of various charge balance mechanisms explains the variability of the vibrational spectroscopic parameters reported in the literature for the B-type carbonates. The position of the ν_{3a} CO_3 band may vary from 1,405 to 1,430 cm^{-1}, whereas the ν_{3b} CO_3 band occurs in the 1,451–1,475 cm^{-1} range (Elliott 1964; Bonel et al. 1973; Featherstone et al. 1984; Sommerauer and Katz-Lehnert 1985; Vignoles et al. 1988; Apfelbaum et al. 1992; Suetsugu et al. 1998; Comodi et al. 1999; Fleet and Liu 2004; Wilson et al. 2004). The position of the ν_{3b} CO_3 band is more difficult to precisely determine as this region usually presents overlapping contributions from A-type and B-type carbonates. The narrower ν_2 CO_3 band can also be used to obtain insights into the CO_3 substitution mechanisms and provides evidences for the occurrence of more than two types of carbonate defects in high-pressure carbonated apatite samples (Fleet 2009). There is a general agreement that the band at ~878 cm^{-1} corresponds to A-type substitution (Elliott 1994) and the band at ~871 cm^{-1} is related to a B-type substitution (e.g., Bonel et al. 1973; Leventouri 2006; Fleet 2009). The clumped (CO_3^{2-}, F^-) defect displays a characteristic narrow band at ~864 cm^{-1} (Yi et al. 2013). This suggests that the B2 signal reported at 864 cm^{-1} by Fleet (2009) is related to the occurrence of the "francolite"-type defect in synthetic carbonated fluorapatite samples. A broader band at ~862 cm^{-1} in biological samples is attributed to a labile component (Rey et al. 1989) but could correspond to a different orientation of A-type channel carbonates (A2-type; Fleet 2009).

The present theoretical results provide specific constraints that could be used to demonstrate or to rule out the occurrence of specific carbonate incorporation mechanism. Consistent with experimental observations, the relative energy of the carbonate defects rules out the occurrence of configurations with vertically orientated carbonate groups. Considering the systematic shift observed between experimental and theoretical wavenumbers and the weak sensibility of ^{13}C NMR values to small modification of the carbonate group environment, bare theoretical vibrational frequencies and ^{13}C NMR chemical shifts cannot be directly used to prove the occurrence of a given defect configuration. In contrast, the splitting of the ν_3 CO_3 bands and the relative position of the ν_2 CO_3 among the defects appear as more relevant parameters. The ^{19}F NMR parameters are also highly sensitive to slight modifications of the environment of fluoride ions. In particular, the theoretical IR and ^{19}F NMR spectroscopic properties of models B_F and A compare very well with those experimentally observed for the "francolite" and A-type carbonate defects, respectively (Tables 2, 3).

Among the investigated models of clumped (CO_3^{2-}, OH^-) defects, the infrared spectroscopic properties of model B_H_1 (local compensation of carbonate group by an hydroxyl group pointing along an edge of the tetrahedral site) unfavorably compare with experimental constraints: the IR calculated spectrum displays a much too low splitting value (14 cm^{-1}) and a too low ν_2 CO_3 wavenumber, which is downshifted by 42 cm^{-1} from the francolite defect. The spectroscopic properties of the closely related B_H_2 model (local compensation of carbonate group by a hydroxyl group pointing out of the tetrahedral site) are in better agreement with experimental IR observations. However, the significantly lower stability (~27 kJ/mol) of B_H_2 with respect to the chemically equivalent B_H_1 model makes it unlikely to occur in apatite samples. In addition, when both F^- and OH^- ions are present in the structure, F^- ions compete successfully for the local charge compensation of carbonate groups at the B-site. Taken together, these observations suggest that a local charge compensation of B-type carbonate groups by hydroxyl ions is unlikely to occur in apatite.

Considering the easy substitution of weakly bonded OH^- groups by F^- ions in a number of minerals (e.g., Robert et al. 1993, 1999) and the very common implication of protons in the charge-compensating mechanisms of cationic vacancies in oxide and silicate minerals (e.g., Bell and Rossman 1992; Keppler and Smyth 2006), the absence of clumped (CO_3^{2-}, OH^-) defects is somehow counter-intuitive. However, it can be understood from qualitative bond valence considerations. In fact, microscopic models of OH groups associated with cationic vacancies in nominally anhydrous minerals have shown that the most stable

configurations correspond to an efficient valence compensation of oxygen atoms through donation and acceptation of hydrogen bonds, such as, in the hydrogarnet (Nobes et al. 2000) or hydrozircon (Balan et al. 2013) defects. In the present case, both the O(9) oxygen of the carbonate group (in B_H_1) and the O(3) oxygen of the neighboring phosphate group (in B_H_2) have their valence fully compensated by the coordinating Ca and P atoms (B_H_2) or Ca and C atoms (B_H_1), making them poor H-bond acceptors. The slightly longest O(H)···O distance (and weaker H-bond) observed in the B_H_1 model is consistent with the greater stability of this model, but in both cases, the presence of an OH group at the apex of the tetrahedral site is significantly less favorable than that of a fluoride ion.

Broadening mechanism of infrared absorption bands of carbonate groups in apatite

The powder infrared spectrum of carbonate-bearing apatite often reveals significant differences in the width of the various bands ascribed to carbonate groups, the ν_3 CO_3 bands being significantly broader than the ν_2 CO_3 band (e.g., Fleet 2009). For example, the average FWHM of the ν_3 CO_3 bands of B-type carbonate in sedimentary carbonate fluorapatite (francolite) is ~20 cm^{-1}, while that of the ν_2 CO_3 band in the same sample is only ~4 cm^{-1} (Yi et al. 2013). In dental enamel, they are ~40 and ~8 cm^{-1}, respectively (e.g., Roche et al. 2010).

The theoretical results presently obtained on the various models of B-type carbonate sites may help to determine the origin of this difference. Besides instrumental resolution, several factors contribute to the width of infrared absorption bands of powdered materials. The homogeneous linewidth is related to the decay of the excited state through anharmonic mode–mode coupling. It leads to Lorentzian band shapes and depends on temperature (Salje et al. 2000). Although measurable, the variation of linewidth of apatite absorption bands with temperature is weak. Thus, homogeneous processes do not appear as the main source of broadening in natural or synthetic apatite samples (Balan et al. 2011; Yi et al. 2013). The inhomogeneous linewidth does not depend on temperature and stems from a distribution of vibrational frequencies within the sample. This distribution can arise from elastic strain fields related to interfaces or point defects, as well as from the occurrence of a nonuniform macroscopic electric field, within the same particle or due to a distribution of particle shapes. For arbitrary particle shapes, the powder absorption bands are usually centered on the frequency computed for spherical particles and display a width similar to the splitting between longitudinal and transverse optical modes (e.g., Balan et al. 2011).

In the case of the weakly absorbing bands of apatite, such as the ν_2 CO_3 or ν_1 PO_4 band, the electrostatic effects are small because the induced polarization is also small. Thus, the linewidth of these bands mostly stems from microscopic inhomogeneous processes. Theoretical mode-Grüneisen parameters provide an assessment of the sensitivity of the vibrational modes to elastic strain fields. From Table 4, the contribution of microscopic distortions to the band broadening should not vary by more than a factor of ~2 between the various absorption bands of B-type carbonate groups. In turn, the significantly larger width experimentally observed for the ν_3 CO_3 modes most likely stems from electrostatic effects related to the dielectric properties of the particles or to long-range interactions between the substituted carbonate defects. Examination of the shift of absorption bands in the spectrum of spherical particles and of the dispersion of the corresponding vibrational modes (assessed from the vibrational frequencies computed at the high-symmetry points of the Brillouin zone, Table 5) indicates that the expected magnitude of these broadening effects is within 10 to a few tens of cm^{-1}. The present theoretical results thus point to previously unrecognized effects contributing to the width and complexity of ν_3 CO_3 absorption bands. Besides the overlap of different signals, these effects modify the band shape and explain why standard fitting approaches may fail to properly account for the ν_3 CO_3 absorption bands in apatite.

Acknowledgments This work was performed using HPC resources from GENCI-IDRIS (Grants 041519 and 091461). Funding by the UPMC Emergence program and the CNRS-INSU "INTERRVIE" program is acknowledged. This is a contribution of LabEx MATISSE.

References

Ames LL (1959) The genesis of carbonate apatites. Econ Geol 54:829–841

Antonakos A, Liarokapis E, Leventouri T (2007) Micro-Raman and FTIR studies of synthetic and natural apatites. Biomaterials 28:3043–3054

Apfelbaum F, Diab H, Mayer I, Featherstone JDB (1992) An FTIR study of carbonate in synthetic apatites. J Inorg Biochem 45:277–282

Astala R, Stott MJ (2005) First principles Investigation of Mineral component of bone: CO_3 substitutions in hydroxyapatite. Chem Mater 17:4125–4133

Balan E, Saitta AM, Mauri F, Calas G (2001) First-principles modeling of the infrared spectrum of kaolinite. Am Mineral 86:1321–1330

Balan E, Delattre S, Roche D, Segalen L, Morin G, Guillaumet M, Blanchard M, Lazzeri M, Brouder C, Salje EKH (2011) Line-broadening effects in the powder infrared spectrum of apatite. Phys Chem Miner 38:111–122

Balan E, Yi H, Blanchard M (2013) First-principles study of OH defects in zircon. Phys Chem Miner 40:547–554

Baroni S, de Gironcoli S, Dal Corso A, Giannozzi P (2001) Phonons and related crystal properties from density-functional perturbation theory. Rev Mod Phys 73:515–561

Bell DR, Rossman GR (1992) Water in the earth's mantle; the role of nominally anhydrous minerals. Science 255:1391–1397

Beshah K, Rey C, Glimcher MJ, Schimizu M, Griffin RG (1990) Solid state ^{13}C and proton NMR-studies of carbonate-containing calcium phosphates and enamel. J Solid State Chem 84:71–81

Bonel G, Labarthe JC, Vignoles C (1973) Contribution à l'étude structurale des apatites carbonates de type B. Colloq Intern CNRS 230:117–125

Comodi P, Liu Y, Stoppa F, Woolley AR (1999) A multi-method analysis of Si-, S- and REE-rich apatite from a new kind of kalsilite-bearing leucitite (Abruzzi, Italy). Miner Mag 63:661–672

De Leeuw N (2002) Density functional theory calculations of local ordering of hydroxy groups and fluoride ions in hydroxyapatite. Phys Chem Chem Phys 4:3865–3871

De Leeuw N (2010) Computer simulations of structures and properties of the biomaterial hydroxyapatite. J Mater Chem 20:5376–5389

Dymek RF, Owens BE (2001) Petrogenesis of apatite-rich rocks (nelsonites and oxide-apatite gabbronorites) associated with massif anorthosites. Econ Geol 96:797–815

Elliott JC (1964) The crystallographic structure of dental enamel, related apatites, PhD thesis, University of London, London

Elliott JC (1994) Structure and chemistry of the apatites and other calcium orthophosphates. Elsevier, Amsterdam

Elliott JC (2002) Calcium phosphate biominerals. In: Kohn ML, Hughes JM (eds) Phosphates—geochemical, geobiological, and materials importance, Reviews in Mineralogy and Geochemistry, Mineralogical Society of America, Chantilly, Virginia, 48: pp. 427-453

Featherstone JDB, Pearson S, LeGeros RZ (1984) An infrared method for quantification of carbonate in carbonated apatites. Caries Res 18:63–66

Fleet ME (2009) Infrared spectra of carbonate apatites: ν_2-region bands. Biomaterials 30:1473–1481

Fleet ME, Liu X (2004) Location of type B carbonate ion in type A–B carbonate apatite synthesized at high pressure. J Solid State Chem 177:3174–3182

Fleet ME, Liu X (2007) Coupled substitution of type A and B carbonate in sodium-bearing apatite. Biomaterials 28:917–926

Fleet ME, Liu X (2008) Accommodation of the carbonate ion in fluorapatite synthesized at high pressure. Am Miner 93:1460–1469

Fleet ME, Liu X, Liu X (2011) Orientation of channel carbonate ions in apatite: effect of pressure and composition. Am Miner 96:1148–1157

Fuchs R (1975) Theory of the optical properties of ionic crystal cubes. Phys Rev B 11:1732–1740

Giannozzi P, Baroni S, Bonini N, Calandra M, Car R, Cavazzoni C, Ceresoli D, Chiarotti GL, Cococcioni M, Dabo I, Dal Corso A, de Gironcoli S, Fabris S, Fratesi G, Gebauer R, Gerstmann U, Gougoussis C, Kokalj A, Lazzeri M, Martin-Samos L, Marzari N, Mauri F, Mazzarello R, Paolini S, Pasquarello A, Paulatto L, Sbraccia C, Scandolo S, Sclauzero G, Seitsonen AP, Smogunov A, Umari P, Wentzcovitch RM (2009) Quantum ESPRESSO: a modular and open-source software project for quantum simulations of materials. J Phys Condens Matter 21:395502

Griffin JM, Yates JR, Berry AJ, Wimperis S, Ashbrook SE (2010) High-Resolution ^{19}F MAS NMR Spectroscopy: structural Disorder and Unusual *J* Couplings in a Fluorinated Hydroxy-Silicate. J Am Chem Soc 132:15651–15660

Grüneisen E (1912) Theorie des fester zustandes einatomiger element. Ann Physik 12:257–306

Hughes JM, Rakovan J (2002) The crystal structure of apatite, $Ca_5(PO_4)_3(F, OH, Cl)$. Rev Miner Geochem 48:1–12

Ivanova TI, Frank-Kamenetskaya OV, Kol'tsov V, Ugolkov L (2001) Crystal structure of calcium-deficient carbonated hydroxyapatite. Thermal decomposition. J Solid state Chem 160:340–349

Keppler H, Smyth JR (eds) (2006) Water in nominally anhydrous minerals. Reviews in Mineralogy and Geochemistry, vol. 62, The Mineralogical Society of America, Chantilly, Virginia

Knudsen AC, Gunter ME (2002) Sedimentary phosphates—An example: Phosphoria formation, Southern Idaho, USA. In: Kohn MJ, Rakovan J Hughes JM (eds) Phosphates Geochemical, Geobiological and Materials Importance. Rev Miner Geochem 14:363–390

Lazzeri M, Thibaudeau P (2006) Ab initio Raman spectrum of the normal and disordered $MgAl_2O_4$ spinel. Phys Rev B 74:140301

LeGeros RZ (1965) Effect of carbonate on the lattice parameters of apatite. Nature 206:403–404

Leventouri Th (2006) Synthetic and biological hydroxyapatites: crystal structure questions. Biomaterials 27:3339–3342

Leventouri Th, Chakoumakos BC, Moghaddam HY, Perdikatsis V (2000) Powder neutron diffraction studies of a carbonate fluorapatite. J Mater Res 15:511–517

Mason HE, Kozlowski A, Phillips BL (2008) Solid-state NMR study of the role of H and Na in AB-type carbonate apatite. Chem Mat 20:294–302

Mason HE, McCubbin FM, Smirnov A, Phillips BL (2009) Solid-State NMR and IR spectroscopic investigation of the role of structural water and F in carbonate-rich fluorapatite. Am Miner 94:507–516

McClellan GH, Lehr JR (1969) Crystal chemical investigation of natural apatite. Am Miner 54:1374–1391

McConnell D (1952) The problem of the carbonate apatites. Structural substitutions involving CO_3 and OH. Bull Soc Fr Miner Cristall 75:428–445

McConnell D (1973) Apatite, its crystal chemistry, mineralogy, and geologic and biologic occurrences. Springer, New York 111p

Michel V, Ildefonse P, Morin G (1995) Chemical and structural changes in Cervus Elaphus tooth enamels during fossilization (Lazaret cave): a combined IR and XRD Rietveld analysis. Appl Geochem 10:145–159

Nobes RH, Akhmatskaya EV, Milman V, White JA, Winkler B, Pickard CJ (2000) An ab initio study of hydrogarnets. Am Mineral 85:1706–1715

Nokhrin SM, Pan Y, Nilges MJ (2006) Electron paramagnetic resonance spectroscopic study of carbonate-bearing fluorapatite: new defect centers and constraints on the incorporation of carbonate ions in apatites. Am Miner 91:1425–1431

Pan Y, Fleet M (2002) Compositions of the apatite-group minerals: substitution mechanisms and controlling factors. In: Kohn MJ, Rakovan J, Hughes JM (eds) Phosphates Geochemical, Geobiological and Materials Importance. Rev Miner Geochem 14:13–50

Pasteris JD, Yoder CH, Sternlieb MP, Liu S (2012) Effect of carbonate incorporation on the hydroxyl content of hydroxylapatite. Min Mag 76:2741–2759

Peeters A, De Maeyer EAP, Van Alsenoy C, Verbeeck RMH (1997) Solids modeled by ab initio crystal-field methods. 12. Structure, orientation and position of A-type carbonate in a hydroxyapatite lattice. J Phys Chem B 101:3995–3998

Perdew JP, Burke K, Ernzerhof M (1996) Generalized gradient approximation made simple. Phys Rev Lett 77:3865–3868

Peroos S, Du Z, de Leeuw NH (2006) A computer modelling study of the uptake, structure and distribution of carbonate defects in hydroxy-apatite. Biomaterials 27:2150–2161

Pickard CJ, Mauri F (2001) All-electron magnetic response with pseudopotentials: NMR chemical shifts. Phys Rev B 63:245101

Rabone JAL, de Leeuw NH (2007) Potential routes to carbon inclusion in apatite minerals: a DFT study. Phys Chem Miner 34:495–506

Regnier P, Berner RA (1996) Mechanism of CO_3^{2-} substitution in carbonate-fluorapatite: evidence from FTIR spectroscopy, ^{13}C NMR, and quantum mechanical calculations-Reply to Nathan. Am Miner 81:515

Regnier P, Lasaga AC, Berner RA, Han OH, Zilm KW (1994) Mechanism of CO_3^{2-} substitution in carbonate-fluorapatite: evidence

from FTIR spectroscopy, ^{13}C NMR, and quantum mechanical calculation. Am Miner 79:809–818

Rey C, Lian J, Grynpas M, Shapiro F, Zylberberg L, Glimcher MJ (1989) Non-apatitic environments in bone mineral: FT-IR detection, biological properties and changes in several disease states. Conn Tiss Res 21:267–273

Robert JL, Della Ventura G, Hawthorne FC (1999) Near-infrared study of short-range disorder of OH and F in monoclinic amphiboles. Am Miner 84:86–91

Robert JL, Beny JM, Della Ventura G, Hardy M (2013) Fluorine in micas: crystal-chemical control of the OH-F distribution between trioctahedral and dioctahedral sites. Eur J Miner 5:7–18

Roche D, Segalen L, Balan E, Delattre S (2010) Preservation assessment of Miocene-Pliocene tooth enamel from Tugen Hills (Kenyan Rift Valley) through FTIR, chemical and stable-isotope analysis. J Archaeol Sci 37:1690–1699

Ruppin R (1977) Infrared absorption in spheroidal crystallites. Surf Sci 62:206–214

Ruppin R (1978) Infrared absorption in rectangular crystallites. Opt Commun 26:360–362

Salje EKH, Carpenter MA, Malcherek T, Boffa Balaran T (2000) Autocorrelation analysis of infrared spectra from minerals. Eur J Miner 12:503–519

Schuffert JD (1990) Carbonate-ion substitution in francolite: a new equation. Geochim Cosmochim Acta 54:2323–2328

Shannon RD (1976) Revised effective ionic radii and systematic studies of interatomic distances in halides and chalcogenides. Acta Cryst A32:751–767

Sommerauer T, Katz-Lehnert K (1985) A new partial substitution mechanism of CO_3^{2-}/CO_3OH^{3-} and SiO_4^{4-} for PO_4^{3-} group in hydroxy-apatite from the Kaiserstuhl alkaline complex. Contrib Miner Petrol 91:360–368

Suetsugu Y, Shimoya I, Tanaka J (1998) Configuration of carbonate ions in apatite structure determined by polarized infrared spectroscopy. J Am Ceram Soc 81:746–748

Tacker RC (2008) Carbonate in igneous and metamorphic fluorapatite: two type A and two type B substitutions. Am Mineral 93:168–176

Ulian G, Valdre G, Corno M, Ugliengo P (2013a) The vibrational features of hydroxylapatite and type A carbonated apatite: a first principle contribution. Am Miner 98:752–759

Ulian G, Valdre G, Corno M, Ugliengo P (2013b). *Ab initio* DFT investigation of structural and vibrational properties of type B and mixed A-B carbonated hydroxylapatite. Am Miner (in press)

Vignoles M, Bonel G, Holcomb DW, Young RA (1988) Influence of preparation conditions on the composition of type B carbonated hydroxyapatite and on the localization of the carbonate ions. Calcif Tissue Int 43:33–40

Wilson RM, Elliott JC, Dowker SEP (1999) Rietveld refinement of the crystallographic structure of human dental enamel apatites. Am Miner 84:1406–1414

Wilson RM, Elliot JC, Dowker SEP, Smith RI (2004) Rietveld structure refinement of precipitated carbonate apatite using neutron diffraction data. Biomaterials 25:2205–2213

Wilson RM, Dowker SEP, Elliot JC (2006) Rietveld refinements and spectroscopic structural studies of a Na-free carbonate apatite made by hydrolysis of monetite. Biomaterials 27:4682–4692

Yi H, Balan E, Gervais C, Segalen L, Fayon F, Roche D, Person A, Morin G, Guillaumet M, Blanchard M, Lazzeri M, Babonneau F (2013) A carbonate-fluoride defect model for carbonate-rich fluorapatite. Am Miner 98:1066–1069